Visible light photocatalytic degradation of dyes by bismuth oxide-reduced graphene oxide composites prepared via microwave-assisted method

Xinjuan Liu [a], Likun Pan [a,*], Tian Lv [a], Zhuo Sun [a], Chang Q. Sun [b]

[a] Engineering Research Center for Nanophotonics & Advanced Instrument, Ministry of Education, Department of Physics, East China Normal University, Shanghai 200062, China
[b] School of Electrical and Electronic Engineering, Nanyang Technological University, Singapore 639798, Singapore

ARTICLE INFO

ABSTRACT

Bi_2O_3-reduced graphene oxide (RGO) composites were successfully synthesized via microwave-assisted reduction of graphite oxide in Bi_2O_3 precursor solution using a microwave system. Their morphologies, structures, and photocatalytic performance in the degradation of methylene blue (MB) and methyl orange (MO) were characterized by scanning electron microscopy, transmission electron microscopy, X-ray diffraction spectroscopy, UV–vis absorption spectroscopy, and electrochemical impedance spectroscopy, respectively. The results show that the RGO addition can enhance the photocatalytic performance of Bi_2O_3–RGO composites. Bi_2O_3–RGO composite with 2 wt.% RGO achieves maximum MO and MB degradation rates of 93% and 96% at 240 min under visible light irradiation, respectively, much higher than those for the pure Bi_2O_3 (78% and 76%). The enhanced photocatalytic performance is ascribed to the increased light adsorption and the reduction in electron–hole pair recombination in Bi_2O_3 with the introduction of RGO.

1. Introduction

Currently, numerous efforts have been made to develop highly effective photocatalysts for the degradation of organic pollutants, selective organic transformation, reduction in heavy metals, air purification, and hydrogen production [1–8]. TiO_2 is recognized to be the most suitable candidates for widespread environmental applications due to its intriguing optical and electric properties, low cost, stability, nontoxicity, and ease of availability [9–11]. Unfortunately, TiO_2 with wide band gap can only exhibit high photocatalytic activity under ultraviolet (UV) light irradiation, which significantly limits its practical applications. To better utilize the solar light which is composed of about 45% of visible light, it is desirable to exploit novel visible light-sensitive semiconductor photocatalysts.

Bi_2O_3 has attracted considerable attention due to its high refractive index, dielectric permittivity, thermal stability and wide application in photocatalysis, gas sensors, capacitors, optical coatings, and photovoltaic cells [12,13]. The band gap of Bi_2O_3 is 2.58–2.85 eV, which has been proved to be good visible light driven photocatalyst for water splitting and pollutant decomposition [14–16]. However, the quick recombination of photo-generated charge carriers has significantly decreased the photocatalytic performance of

Bi_2O_3 [14,17]. Graphene is an emerging carbon material with a unique two-dimensional conjugated chemical structure, which has attracted a great deal of attention in recent years owing to its excellent conductivity, superior chemical stability, and high specific surface area [18–22]. Chemical approaches via reduction of graphite oxide (GO), for the large-scale production of graphene (normally called as reduced graphene oxide (RGO)) sheets, have become reality, which speeds up the application of graphene in photocatalysis [23,24], energy storage [25], and solar cells [26]. Currently, many studies have reported that the integration of RGO and semiconductor photocatalyst, such as ZnO, TiO_2, CdS, and ZnS, could obtain hybrid materials with superior photocatalytic activity [27–36]. Xu et al. [9] prepared ZnO–graphene composite by reducing GO coated on the surface of ZnO nanoparticles using hydrazine and found that the ZnO–graphene composite showed an improved photocatalytic performance in the degradation of organic dye as compared with pure ZnO. Guo et al. [37] revealed that TiO_2–graphene composites prepared by sono-chemical method displayed better photocatalytic performance for the degradation of methylene blue (MB) than commercial pure TiO_2. In our previous works, we fabricated ZnO–RGO [38], TiO_2–RGO [39], and CdS–RGO [40] composites by microwave-assisted reduction of GO in ZnO, TiO_2, and CdS precursor solution, respectively, and the composites exhibited better photocatalytic performance in the reduction of Cr(VI) under UV or visible light irradiation as compared with pure ZnO, TiO_2 or CdS. The significant enhancement of

---

* Corresponding author. Fax: +86 21 62234321.
  E-mail address: lkpan@phy.ecnu.edu.cn (L. Pan).

photocatalytic performance of these composites arises from that RGO can act as an excellent electron-acceptor/transport material to effectively facilitate the migration of photo-induced electrons and hinder the charge recombination in electron-transfer processes due to the electronic interaction between photocatalyst and RGO [9,20,41]. Recently, Zhang et al. [36] proposed a new photocatalytic mechanism where the role of RGO in the ZnS–RGO composites acts as an organic dye-like macromolecular photosensitizer for ZnS instead of an electron reservoir. Based on the above progress, the combination of RGO and Bi_2O_3 should be a promising method to enhance the visible light photocatalytic performance of Bi_2O_3. Unfortunately, up to now, the exploration on Bi_2O_3–RGO composites has not yet been reported.

In this work, we reported a one-step synthesis of Bi_2O_3–RGO composites through microwave-assisted reduction of GO in Bi_2O_3 precursor solution using a microwave system, and their photocatalytic performances in the degradation of MB and methyl orange (MO) under visible light irradiation were investigated. Microwave irradiation can heat the reactant to a high temperature in a short time by transferring energy selectively to microwave absorbing polar solvents. Thus, it can facilitate mass production in a short time with little energy cost [42] and form a intimate contact between the components [38,40,43], which is crucial for the carrier transportation and separation. Such a microwave-assisted reaction has hardly been employed to synthesize Bi_2O_3–RGO composites although it has been used successfully to fabricate RGO [44] and Bi_2O_3 [45], respectively.

2. Experimental

2.1. Synthesis of Bi₂O₃–RGO composite

Commercial graphite powder was used as the starting reagent for the synthesis of GO via modified Hummers method, which has been described in our previous works [39,40,46,47]. 0.1 mmol $Bi(NO_3)_3$ was dissolved in 20 ml nitric acid (1.5 mol/l) to avoid the hydrolyzation of Bi^{3+} ions because the nitric acid can prevent the formation of the precipitation of $BiONO_3$ [48,49]. Then, a certain amount of 24 mg ml^{-1} GO suspension was added into $Bi(NO_3)_3$ solution, which was placed in a 35 ml microwave tube, and then, the solution was sonicated for 30 min to produce uniform dispersion. A dilute NaOH solution was dropped in the solution to form a brownish-black suspension with a pH value of 7. The mixture was then put into an automated focused microwave system (Explorer-48, CEM Co.) and treated at 150 °C with microwave irradiation power of 150 W for 10 min. It was obviously found that the color of suspension had changed into grayish-black, indicating the chemical reduction in GO sheets [50]. The as-synthesized Bi_2O_3–RGO samples with 1, 2, and 3 wt.% RGO, named as BG-1, BG-2, and BG-3, were isolated by filtration, washed for three times with distilled water, and finally dried in a vacuum oven at 60 °C for 24 h. Pure Bi_2O_3 and RGO were also synthesized by direct microwave-assisted reaction for comparison. For the electrochemical impedance spectra (EIS) testing, the as-synthesized composites with 5 wt.% cellulose binder were homogenously mixed in terpineol to form a slurry. Then, the resultant slurries were coated on the FTO using a screen-printing approach. The thickness and area of the screen printed layers is 2.5 μm and 8 cm^2. Finally, these prepared electrodes were dried at 100 °C for 30 min and sintered at 500 °C for 30 min.

2.2. Characterization

The surface morphology, structure, and composition of the samples were characterized by field-emission scanning electron microscopy (FESEM, Hitachi S-4800), high-resolution transmission electron microscopy (HRTEM, JEOL-2010), X-ray diffraction spectroscopy (XRD, Holland Panalytical PRO PW3040/60) with Cu Kα radiation (V = 30 kV, I = 25 mA), and energy dispersive X-ray spectroscopy (EDS, JEM-2100), respectively. The UV–vis absorption spectra were recorded using a Hitachi U-3900 UV–vis spectrophotometer. Brunauer–Emmett–Teller (BET) specific surface areas (S_{BET}) of the samples were evaluated on the basis of nitrogen adsorption isotherms measured at 77 K using a BELSORP-max nitrogen adsorption apparatus (Japan Inc.). All the samples were degassed at 150 °C before nitrogen adsorption measurements. The BET surface area was determined using the adsorption data in the relative pressure (P/P_0) range of 0.05–0.35. EIS measurements were carried out on an electrochemical workstation (AUTO-LAB PGSTAT302N) under the illuminated condition using a three electrode configuration with the as-prepared films as working electrode, a Pt foil as counter electrode, and a standard calomel electrode as reference electrode. The electrolyte was 5 mg l^{-1} MO aqueous solution. EIS were recorded in the frequency range of 0.01 Hz–1 MHz, and the applied bias voltage and ac amplitude were set at open-circuit voltage and 10 mV AC between the counter electrode and the working electrode, respectively.

2.3. Photocatalytic experiments

The photocatalytic performance of the as-prepared samples was evaluated through the photocatalytic degradation of MO and MB under visible light irradiation, respectively. The samples (2 g l^{-1}) were dispersed in 80 ml MB aqueous solutions (5 mg l^{-1}) and 80 ml MO aqueous solutions (5 mg l^{-1}), respectively. The mixed suspensions were first magnetically stirred in the dark for 30 min to reach the adsorption–desorption equilibrium. Under the ambient conditions and stirring, the mixed suspensions were exposed to visible light irradiation produced by a 400 W metal halogen lamp (λ > 400 nm) in a photocatalytic equipment with water cooling device (Shang Hai Bilon Instruments Co., Ltd). At certain time intervals, 2 ml of the mixed suspensions was centrifuged to remove the photocatalyst and analyzed by recording UV–vis spectra of MB and MO using a Hitachi U-3900 UV–vis spectrophotometer. The normalized temporal concentration changes (C/C_0) of MB and MO during the photocatalytic process are proportional to the normalized maximum absorbance (A/A_0), which can be derived from the change in the MB and MO absorption profile at a given time interval. The degradation rate is calculated as the following equation:

3. Results and discussion

Fig. 1(a and b) shows the FESEM images of the as-synthesized RGO and Bi_2O_3. The RGO nanosheets are curled and corrugated, and Bi_2O_3 displays the rod nanostructure. C/O ratio is often used as a convenient measurement of the oxidation degree of GO samples. Previous results have been reported that the C/O ratio changes from 2 to 10 [51–53], after microwave irradiation, indicating the efficient deoxygenation of GO and the formation of graphene. Fig. 1(c) displays the FESEM image of BG-3. The morphologies of BG-1 and BG-2 (not shown here) are similar to that of BG-3. It is clearly observed in Fig. 1(c) that the RGO sheets are decorated densely by Bi_2O_3 nanorods, which displays a good combination between them. The composition of BG-3 was identified by EDS linked to FESEM, as shown in Fig. 1(d). The peaks of Bi and O in the EDS profile prove the existence of Bi_2O_3 in the composite. The appearance of Na element is due to the residue of reactants during the synthesis. Fig. 1(e and f) shows the HRTEM images of Bi_2O_3 and BG-3. It is clearly seen that Bi_2O_3 is relatively uniform,
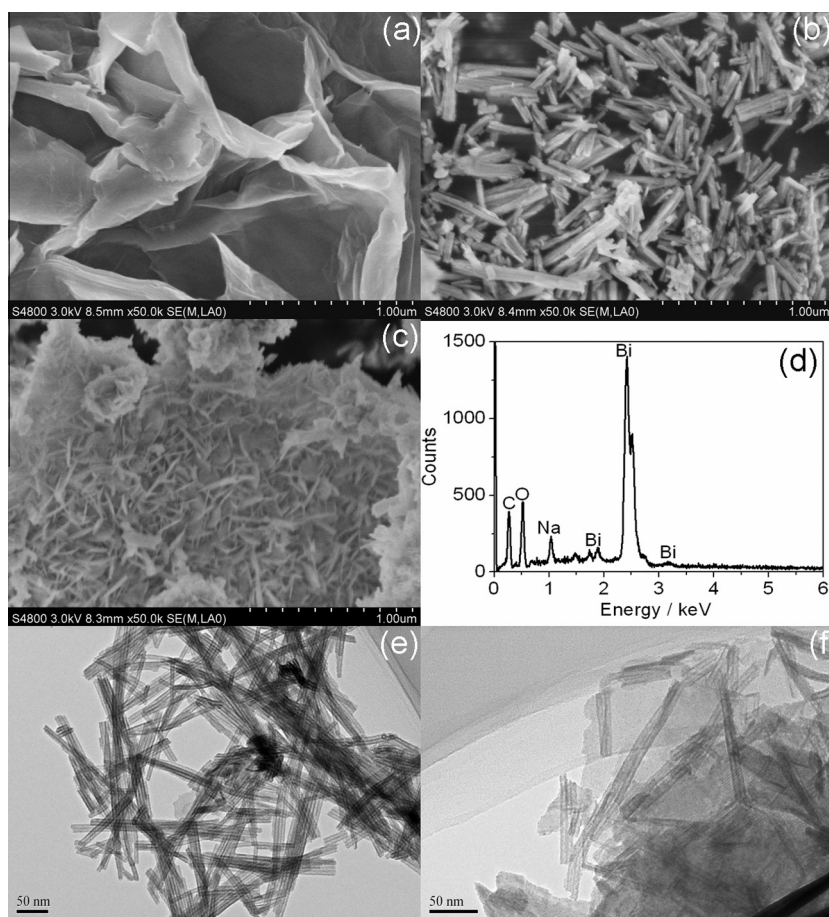
Fig. 1. FESEM images of (a) RGO nanosheets, (b) Bi_2O_3 nanorods and (c) BG-3; (d) EDS spectrum of BG-3; HRTEM images of (e) Bi_2O_3 nanorods and (f) BG-3.

dispersive, and rod morphology with diameter in the range of 10–40 nm. When RGO nanosheets are incorporated into Bi_2O_3, as illustrated in Fig. 1(f), Bi_2O_3 nanorods are observed to be attached onto the surface of RGO sheets.

The XRD patterns of RGO, Bi_2O_3, and BG-3 are shown in Fig. 2. RGO nanosheets exhibit a strong (002) diffraction peak at 26° [54]. The diffraction pattern of Bi_2O_3 shows that all the peaks can be indexed as the cubic crystal structure of the γ-Bi_2O_3 (JCPDS 6-312), and no other impurity phases are found, indicating the good phase purity of the products. The XRD analysis indicates that all the diffraction peaks of BG-3 are similar to those of pure Bi_2O_3, which demonstrates that the presence of RGO does not result in the development of new crystal orientations or changes in preferential orientations of Bi_2O_3. No typical diffraction peaks of carbon

species for BG-3 are observed, which is due to the low content of RGO below the detection limit [41].

The UV–vis absorption spectra of Bi_2O_3, BG-1, BG-2, and BG-3 are shown in Fig. 3. The Bi_2O_3 shows spectral response in a wide range from UV to visible light. Pure RGO exhibits a weak absorption peak at 262 nm, as shown in the inset of Fig. 3, which is generally attributed to the excitation of π-plasmon of the graphitic structure [40,55]. Compared with pure Bi_2O_3, the absorbance of Bi_2O_3–RGO composite increases with the increase in the RGO content, which may be due to the absorption contribution from RGO, the increase in surface electric charge of the oxides and modification of the fundamental process of electron–hole pair formation during irradiation [9,35,56]. The obtained result is similar with previous reports [9,30,31,56,57]. Therefore, the presence of RGO
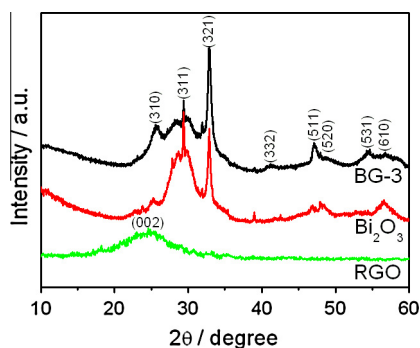
Fig. 2. XRD patterns of RGO, Bi_2O_3 and BG-3.
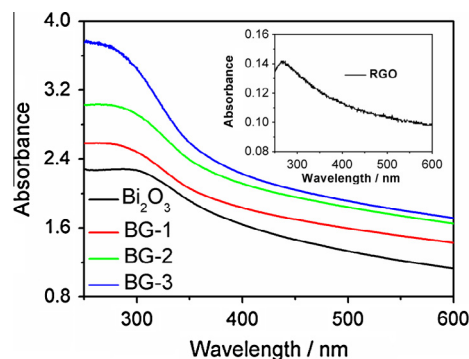
Fig. 3. UV–vis absorption spectra of RGO (inset), Bi_2O_3, BG-1, BG-2, and BG-3.

in Bi_2O_3 can increase the light absorption intensity, which is beneficial for the photocatalytic performance. Furthermore, the band gaps of Bi_2O_3, BG-1, BG-2, and BG-3 by extrapolating the linear portion of the curve to zero absorbance are 2.68, 2.63, 2.61, and 2.72 eV, which shows that Bi_2O_3 and Bi_2O_3–RGO composite synthesized via microwave-assisted method can be excited by visible light and may exhibit good visible light photocatalytic activities.

The charge transfer and recombination behavior of the as-prepared samples were studied by analyzing the EIS spectra at open-circuit voltage under the illuminated condition. Fig. 4 shows the typical Nyquist plots of FTO, Bi_2O_3, BG-1, BG-2, and BG-3. The semicircle in the EIS spectra is due to the contribution from the charge transfer resistance (R_{ct}) and constant phase element (CPE). The R_{ct} should be resulted from the resistances at the interface between electrolyte and electrode and inside the electrode. The corresponding equivalent circuit is shown in the inset of Fig. 4. It can be observed that the R_{ct} of pure FTO is larger than pure Bi_2O_3 and Bi_2O_3–RGO composite. The R_{ct} decreases with the increase in RGO content, indicating that the introduction of RGO suppresses the charge recombination, which is beneficial to photocatalysis [9,31,32,41,58]. Furthermore, the conduction band of Bi_2O_3 is 0.33 V and valence band 3.13 V (vs. NHE) [59]. The work function of RGO is −0.08 V (vs. NHE) [22]. Therefore, RGO in the Bi_2O_3–RGO composite may act as an organic dye-like macromolecular photosensitizer for Bi_2O_3, which is similar with previous report [36]. However, when the RGO content is further increased (BG-3), the R_{ct} increases, which is may because that excessive RGO can act as recombination center and promote the recombination of electron–hole pairs in RGO [57,60].

Photocatalytic degradation of MO by Bi_2O_3, BG-1, BG-2, and BG-3 was performed under visible light irradiation. Fig. 5(a) shows the UV–vis absorbance of MO with irradiation time under visible light irradiation using BG-2. It is observed that the UV–vis absorption peak of MO, related to the concentration of MO in the solution, becomes weak with the increase in the irradiation time. The shape of the absorption spectrum of the dye does not vary during the photocatalytic process. The wavelength at which absorbance readings are made is 463 nm. The normalized temporal concentration changes (C/C_0) of MO during the photocatalytic process are proportional to the normalized maximum absorbance (A/A_0), which can be derived from the change in the MO absorption profile at a given time interval.

Fig. 5(b) displays the time-dependent degradation rates of MO by Bi_2O_3, BG-1, BG-2, and BG-3 under visible light irradiation. It is observed that the concentration of MO is hardly reduced under visible light irradiation in the absence of the photocatalyst and Bi_2O_3–RGO composites exhibit better photocatalytic performance than pure Bi_2O_3. The photocatalytic performance of Bi_2O_3–RGO composites is dependent on the proportion of RGO in the

Fig. 5. (a) UV–vis absorbance of MO with irradiation time under visible light irradiation using BG-2, (b) Photocatalytic degradation of MO by Bi_2O_3, BG-1, BG-2, and BG-3 under visible light irradiation, and (c) the photocatalytic reaction kinetics of MO with reaction time.

composites. However, it can be observed that some of degradation rate cross. It should be ascribed to the high rate constant, which is possibly related to the high MO concentration on the surface of photocatalyst when the photocatalysis begins after dark reaction [61]. The degradation rate of MO for pure Bi_2O_3 is 78%. When RGO is introduced into Bi_2O_3, the degradation rate is increased to 81% for BG-1 and reaches a maximum value of 93% for BG-2 at 240 min. It is known that during photocatalysis, the adsorption of pollutants, the light harvesting, and the charge transportation and separation are crucial factors [38,41]. Compared with Bi_2O_3 and BG-1, BG-2, and BG-3 exhibit a higher absorbance in the visible light range, resulting in an increase in the number of photo-generated electrons and holes to participate in the photocatalytic reaction, which has been confirmed by the UV–vis absorption spectra. Therefore, BG-2 and BG-3 exhibit a better photocatalytic performance than Bi_2O_3 and BG-1. Furthermore, BG-2 exhibits a lowest R_{ct}, indicating that the recombination of photo-induced electrons and holes in BG-2 is most effectively inhibited, which has been confirmed by the EIS measurement. Therefore, among
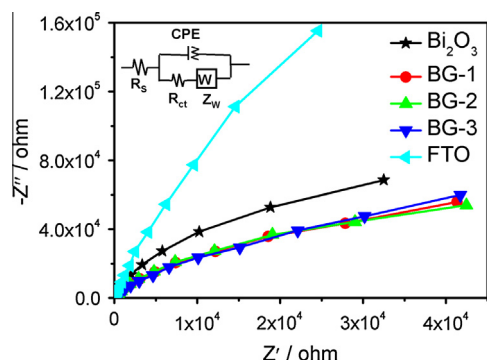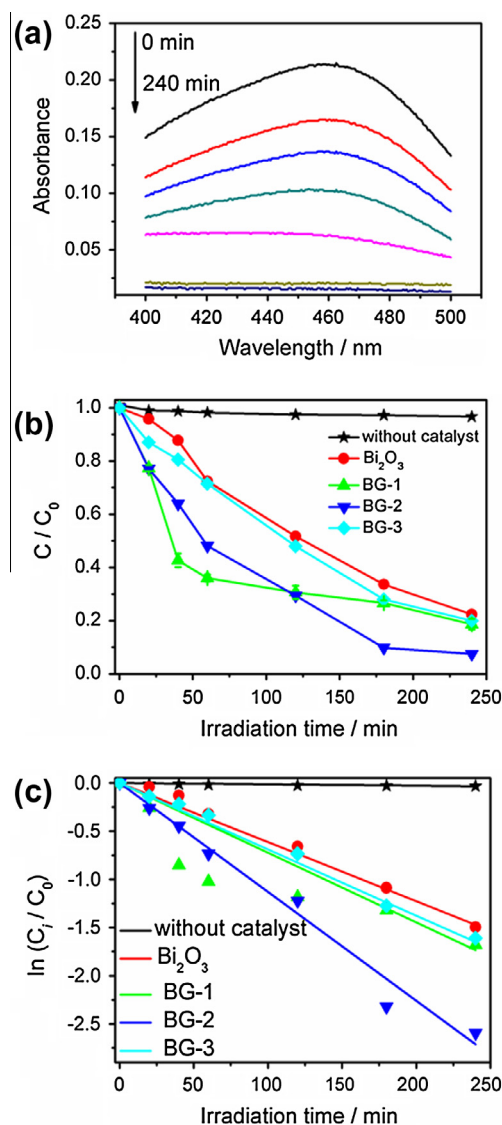

Fig. 4. Nyquist plots of FTO, Bi_2O_3, BG-1, BG-2, and BG-3. Inset is the corresponding equivalent circuit model.

all samples, BG-2 exhibits the best photocatalytic performance under visible light irradiation. The BET measurement result shows that the specific surface areas of Bi_2O_3 and BG-2 are 11.6 and 24.6 $m^2 g^{-1}$, respectively, which indicates that the incorporation of RGO increases the specific surface area of the composite and can enhance the adsorption of MO. Therefore, the enhancement of the photocatalytic performance should be ascribed to the increase in the amount of adsorbed MO, the light harvesting and the reduction in electron–hole pair recombination in Bi_2O_3 with the presence of RGO. Furthermore, the self-sensitized degradation of the dyes should also play a critical role in the improvement of photocatalytic performance of Bi_2O_3 under visible light irradiation [46]. MO is excited under visible light irradiation to MO*, followed by photo-induced electrons transfer from MO* to Bi_2O_3, which react with adsorbed oxidants, usually O_2, to produce reactive oxygen radicals (O_2^-) [46,62]. The increase in the amount of adsorbed MO can cause its more efficient self-sensitized degradation, which leads to the enhancement of photocatalytic performance. However, the degradation rate of Bi_2O_3–RGO composite with 3 wt.% RGO decreases to 80%. This is possibly because (i) excessive RGO in composite increases the opportunity for the collision of electrons and holes and acts as a kind of recombination center, leading to the promotion of the recombination of electron–hole pair in RGO [40,57,60,63] and (ii) RGO simply filters light and decreases the number of charge carriers in the composite to be photo-generated [46]. Furthermore, the photo-stability of BG-1 by investigating its photocatalytic performance with three times of cycling uses was studied. The error bar was provided in Fig. 5(b). It can be seen that the recycled use of BG-1 for three times does not conspicuously affect its photocatalytic activity, which reveals that the composite is stable under the studied conditions.

Fig. 5(c) shows the linear fitting between pseudo-first-order kinetic equation and experimental data for Bi_2O_3, BG-1, BG-2, and BG-3. The values of rate constant (k) can be obtained directly from the fitted straight-line plots of $\ln(C_i/C_0)$ vs. reaction time. The values of k in the absence of the photocatalyst is 0.00014 min^{-1}, indicating that MO can almost not be reduced in the dark reaction, which ensures the effect of physical adsorption of MO to be eliminated. Furthermore, the values of k under visible light irradiation follow the order: BG-2 (0.0113 min^{-1}) > BG-1 (0.0072 min^{-1}) > BG-3 (0.0069 min^{-1}) > Bi_2O_3 (0.0061 min^{-1}). The result shows that BG-2 exhibits a best photocatalytic activity under visible light irradiation. It can be seen that several experimental points shown in Fig. 5(c) deviate from the linear correlation. The discrepancies between model and experimental data should be ascribed to the high rate constant at initial reaction time and the low rate constant at subsequent reaction time, which is similar with previous reports [64–66]. The high rate constant at initial reaction time is possibly related to the high MO concentration on the surface of photocatalyst when the photocatalysis begins after dark reaction [61].

In order to investigate the generality of the photocatalysis for the removal of other pollutants, photocatalytic degradation of MB under visible light irradiation was carried out, as shown in Fig. 6. It is observed that the concentration of MB is hardly reduced under visible light irradiation in the absence of the photocatalyst. The degradation rates of MB for pure Bi_2O_3 and RGO are 76% and 15%, respectively. When RGO is introduced into Bi_2O_3, the degradation rate reaches 96% for BG-2 at 240 min. The result is similar to that for MO degradation. Therefore, it is obvious that a remarkable synergistic contributions from Bi_2O_3 and RGO, leading to high photocatalytic activities in the degradation of MO and MB.

The good contact between Bi_2O_3 and RGO is essential for the quick transfer of photogenerated electrons during the photocatalytic reaction. In this work, the sample with 2 wt.% RGO (BG-2-m) was also prepared by simple mechanical mixing of Bi_2O_3 and RGO and its photocatalytic activities in the degradation of MO
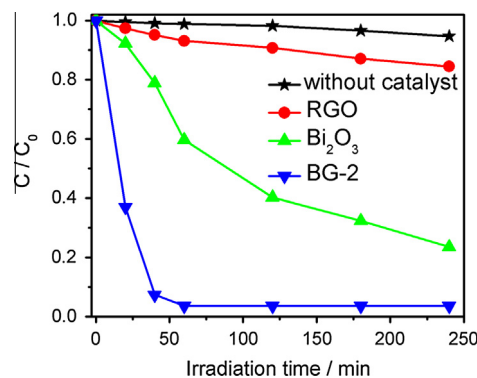

Fig. 6. Photocatalytic degradation of MB by Bi_2O_3, RGO and BG-2 under visible light irradiation.
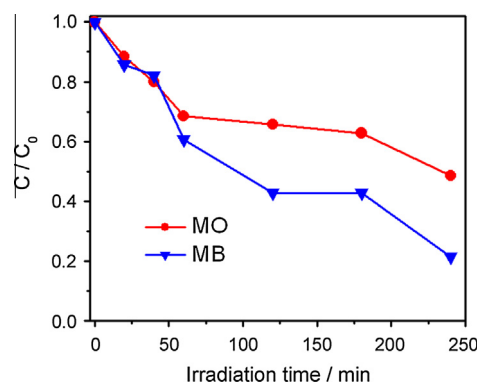

Fig. 7. Photocatalytic degradation of MO and MB by BG-2-m under visible light irradiation.

and MB under visible light irradiation were examined, as shown in Fig. 7. It can be observed that the degradation rates of MO (52%) and MB (79%) for the BG-2-m obtained by direct mixing are much lower than those for the BG-2 fabricated via microwave-assisted synthesis method. The results indicate that microwave-assisted synthesis is beneficial to the formation of good contact between Bi_2O_3 and RGO, which can facilitate the carrier transfer between Bi_2O_3 and RGO and inhibit the interfacial carrier recombination [67].

4. Conclusions

Bi_2O_3–RGO composites were successfully synthesized via microwave-assisted reduction of GO in Bi_2O_3 precursor solution using a microwave system and their photocatalytic performances under visible light irradiation were investigated. The results indicate that (i) the Bi_2O_3–RGO composites exhibit an enhanced photocatalytic performance in the degradation of dyes as compared with pure Bi_2O_3 and their photocatalytic performances are dependent on the proportion of RGO in the composites; (ii) the Bi_2O_3–RGO composite with 2 wt.% RGO achieves a highest MO degradation rate of 93% and a MB degradation rate of 96% at 240 min; (iii) the enhanced photocatalytic performance is ascribed to the increased adsorption and light harvesting as well as the reduction in photoelectron–hole pair recombination in Bi_2O_3 with the introduction of RGO. The semiconductor photocatalyst doped with RGO should be a promising visible light photocatalyst for treating the dye wastewater.

Acknowledgments

References

[1] Q. Shen, W. Zhang, Z.P. Hao, L.D. Zou, Chem. Eng. J. 165 (2010) 301–309.
[2] F.Y. Shen, W.X. Que, Y.L. Liao, X.T. Yin, Ind. Eng. Chem. Res. 50 (2011) 9131–9137.
[3] M.Y. Xing, Y.M. Wu, J.L. Zhang, F. Chen, Nanoscale 2 (2010) 1233–1239.
[4] N. Zhang, Y.H. Zhang, Y.J. Xu, Nanoscale 4 (2012) 5792–5813.
[5] Y.H. Zhang, Z.R. Tang, X.Z. Fu, Y.J. Xu, ACS Nano 5 (2011) 7426–7435.
[6] Y.H. Zhang, N. Zhang, Z.R. Tang, Y.J. Xu, Phys. Chem. Chem. Phys. 14 (2012) 9167–9175.
[7] N. Zhang, Y.H. Zhang, X.Y. Pan, X.Z. Fu, S.Q. Liu, Y.J. Xu, J. Phys. Chem. C 115 (2011) 23501–23511.
[8] N. Zhang, Y.H. Zhang, X.Y. Pan, M.Q. Yang, Y.J. Xu, J. Phys. Chem. C 116 (2012) 18023–18031.
[9] T.G. Xu, L.W. Zhang, H.Y. Cheng, Y.F. Zhu, Appl. Catal. B: Environ. 101 (2011) 382–387.
[10] S.S. Zhang, F. Peng, H.J. Wang, H. Yu, S.Q. Zhang, J. Yang, H.J. Zhao, Catal. Commun. 12 (2011) 689–693.
[11] Y.L. Liao, W.X. Que, Z.H. Tang, W.J. Wang, W.H. Zhao, J. Alloys Compd. 509 (2011) 1054–1059.
[12] Z.H. Ai, Y.H. Huang, S.C. Lee, L.Z. Zhang, J. Alloys Compd. 509 (2011) 2044–2049.
[13] H.B. Lu, S.M. Wang, L. Zhao, B.H. Dong, Z.X. Xu, J.C. Li, RSC Adv. 2 (2012) 3374–3378.
[14] X.W. Liu, H.Q. Cao, J.F. Yin, Nano Res. 4 (2011) 470–482.
[15] Y.F. Qiu, M.L. Yang, H.B. Fan, Y.Z. Zuo, Y.Y. Shao, Y.J. Xu, X.X. Yang, S.H. Yang, CrystEngComm 13 (2011) 1843–1850.
[16] Z.L. Xu, I. Tabata, K. Hirogaki, K. Hisada, T. Wang, S. Wang, T. Hori, Catal. Sci. Technol. 1 (2011) 397–400.
[17] G.Q. Zhu, W.X. Que, J. Zhang, J. Alloys Compd. 509 (2011) 9479–9486.
[18] X.R. Wang, X.L. Li, L. Zhang, Y.K. Yoon, P.K. Weber, H.L. Wang, J. Guo, H.J. Dai, Science 324 (2009) 768–771.
[19] Q.J. Xiang, J.G. Yu, M. Jaroniec, Chem. Soc. Rev. 41 (2012) 782–796.
[20] K.F. Zhou, Y.H. Zhu, X.L. Yang, X. Jiang, C.Z. Li, New J. Chem. 35 (2011) 353–359.
[21] J.T. Zhang, Z.G. Xiong, X.S. Zhao, J. Mater. Chem. 21 (2011) 3634–3640.
[22] Q.J. Xiang, J.G. Yu, M. Jaroniec, Nanoscale 3 (2011) 3670–3678.
[23] B.J. Li, H.Q. Cao, J. Mater. Chem. 21 (2011) 3346–3349.
[24] A. Iwase, Y.H. Ng, Y. Ishiguro, A. Kudo, R. Amal, J. Am. Chem. Soc. 133 (2011) 11054–11057.
[25] L.L. Zhang, R. Zhou, X.S. Zhao, J. Mater. Chem. 20 (2010) 5983–5992.
[26] G. Zhu, L.K. Pan, T. Lu, T. Xu, Z. Sun, J. Mater. Chem. 21 (2011) 14869–14875.
[27] T. Lv, L.K. Pan, X.J. Liu, T. Lu, G. Zhu, Z. Sun, J. Alloys Compd. 509 (2011) 10086–10091.
[28] Y.H. Zhang, Z.R. Tang, X.Z. Fu, Y.J. Xu, ACS Nano 2 (2010) 7303–7314.
[29] Y.H. Ng, A. Iwase, A. Kudo, R. Amal, J. Phys. Chem. Lett. 1 (2010) 2607–2612.
[30] Y.L. Min, K. Zhang, Y.C. Chen, Y.G. Zhang, Sep. Purif. Technol. 86 (2012) 98–105.
[31] J.J. Guo, Y. Li, S.M. Zhu, Z.X. Chen, Q.L. Liu, D. Zhang, W.J. Moon, D.M. Song, RSC Adv. 2 (2012) 1356–1363.
[32] Y.S. Fu, X. Wang, Ind. Eng. Chem. Res. 50 (2011) 7210–7218.
[33] L. Jia, D.H. Wang, Y.X. Huang, A.W. Xu, H.Q. Yu, J. Phys. Chem. C 115 (2011) 11466–11473.
[34] H.T. Hu, X.B. Wang, F.M. Liu, J.C. Wang, C.H. Xu, Synthetic Met. 161 (2011) 404–410.
[35] Y.F. Sun, B.Y. Qu, Q. Liu, S. Gao, Z.X. Yan, W.S. Yan, B.C. Pan, S.Q. Wei, Y. Xie, Nanoscale 4 (2012) 3761–3767.
[36] Y.H. Zhang, N. Zhang, Z.R. Tang, Y.J. Xu, ACS Nano 6 (2012) 9777–9789.
[37] J.J. Guo, S.M. Zhu, Z.X. Chen, Y. Li, Z.Y. Yu, Q.L. Liu, J.B. Li, C.L. Feng, D. Zhang, Ultrason. Sonochem. 18 (2011) 1082–1090.
[38] X.J. Liu, L.K. Pan, T. Lv, T. Lu, G. Zhu, Z. Sun, C.Q. Sun, Catal. Sci. Technol. 1 (2011) 1189–1193.
[39] X.J. Liu, L.K. Pan, T. Lv, G. Zhu, T. Lu, Z. Sun, C.Q. Sun, RSC Adv. 1 (2011) 1245–1249.
[40] X.J. Liu, L.K. Pan, T. Lv, G. Zhu, Z. Sun, C.Q. Sun, Chem. Commun. 47 (2011) (1986) 11984–11986.
[41] H. Zhang, X.J. Lv, Y.M. Li, Y. Wang, J.H. Li, ACS Nano 4 (2010) 380–386.
[42] A.V. Murugan, T. Muraliganth, A. Manthiram, Chem. Mater. 21 (2009) 5004–5006.
[43] G. Zhu, L.K. Pan, T. Xu, Q. Zhao, B. Lu, Z. Sun, Nanoscale 3 (2011) 2188–2193.
[44] B.G. Choi, H. Park, M.H. Yang, Y.M. Jung, S.Y. Lee, W.H. Hong, T.J. Park, Nanoscale 2 (2010) 2692–2697.
[45] Q.Q. Huang, S.N. Zhang, C.X. Cai, B. Zhou, Mater. Lett. 65 (2011) 988–990.
[46] T. Lv, L.K. Pan, X.J. Liu, T. Lu, G. Zhu, Z. Sun, C.Q. Sun, Catal. Sci. Technol. 2 (2012) 754–758.
[47] T. Lu, L.K. Pan, H.B. Li, G. Zhu, T. Lv, X.J. Liu, Z. Sun, T. Chen, D.H.C. Chua, J. Alloys Compd. 509 (2011) 5488–5492.
[48] H. Zhang, Y.J. Ji, X.Y. Ma, J. Xu, D.R. Yang, Nanotechnology 14 (2003) 974–977.
[49] A.P. Zhang, J.Z. Zhang, N.Y. Cui, X.Y. Tie, Y.W. An, L.J. Li, J. Mol. Catal. A: Chem. 304 (2009) 28–32.
[50] H.A. Becerril, J. Mao, Z. Liu, R.M. Stoltenberg, Z. Bao, Y. Chen, ACS Nano 2 (2008) 463–470.
[51] T. Lu, L.K. Pan, C.Y. Nie, Z.J. Zhao, Z. Sun, Phys. Status Solidi A 208 (2011) 2325.
[52] T.Q. Chen, L.K. Pan, K. Yu, Z. Sun, Solid State Ionics 229 (2012) 9–13.
[53] J.F. Shen, T. Li, Y. Long, M. Shi, N. Li, M.X. Ye, Carbon 50 (2012) 2134–2140.
[54] L.H. Tang, Y. Wang, Y.M. Li, H.B. Feng, J. Lu, J.H. Li, Adv. Funct. Mater. 19 (2009) 2782–2789.
[55] J.L. Wu, S. Bai, X.P. Shen, L. Jiang, Appl. Surf. Sci. 257 (2010) 747–751.
[56] E. Gao, W.Z. Wang, M. Shang, J.H. Xu, Phys. Chem. Chem. Phys. 13 (2011) 2887–2893.
[57] H.W. Ma, J.F. Shen, M. Shi, X. Lu, Z.Q. Li, Y. Long, N. Li, M.X. Ye, Appl. Catal. B: Environ. 121–122 (2012) 198–205.
[58] Y.S. Fu, X.Q. Sun, X. Wang, Mater. Chem. Phys. 131 (2011) 325–330.
[59] C.Z. Li, J.Y. Zhang, K.J. Liu, Int. J. Electrochem. Sci. 7 (2012) 5028–5034.
[60] N.L. Yang, J. Zhai, D. Wang, Y.S. Chen, L. Jiang, ACS Nano 4 (2010) 887–894.
[61] X.J. Liu, T. Lv, L.K. Pan, Z. Sun, C.Q. Sun, Desal. Wat. Treat. 42 (2012) 216–221.
[62] Z.G. Xiong, L.L. Zhang, J.Z. Ma, X.S. Zhao, Chem. Commun. 46 (2010) 6099–6101.
[63] X.Y. Zhang, H.P. Li, X.L. Cui, Y.H. Lin, J. Mater. Chem. 20 (2010) 2801–2806.
[64] W.J. Huang, G.C. Fang, C.C. Wang, Colloids Surf. A: Physicochem. Eng. Asp. 260 (2005) 45–51.
[65] S.F. Chen, W. Liu, H.Y. Zhang, X.L. Yu, J. Hazard. Mater. 186 (2011) 1687–1695.
[66] R. Asapu, V.M. Palla, B. Wang, Z. Guo, R. Sadu, D.H. Chen, J. Photochem. Photobiol. A: Chem. 225 (2011) 81–87.
[67] G. Zhu, L.K. Pan, T. Xu, Z. Sun, ACS Appl. Mater. Interfaces 3 (2011) 3146–3151.